Journal of Zhejiang University-SCIENCE A (Applied Physics & Engineering)
ISSN 1673-565X (Print); ISSN 1862-1775 (Online)
www.zju.edu.cn/jzus; www.springerlink.com
E-mail: jzus@zju.edu.cn

Simulation methodology development for rotating blade containment analysis*

Qing HE[1], Hai-jun XUAN[†‡1], Lian-fang LIAO[2], Wei-rong HONG[1], Rong-ren WU[1]

([1]*High-Speed Rotating Machinery Laboratory, Institute of Chemical Machinery, Zhejiang University, Hangzhou 310027, China*)

([2]*Department of Automation, Zhejiang University, Hangzhou 310027, China*)

[†]E-mail: marine@zju.edu.cn

Received Nov. 1, 2011; Revision accepted Feb. 22, 2012; Crosschecked Feb. 27, 2012

Abstract: An experimental and numerical investigation on the aeroengine blade/case containment analysis is presented. Blade out containment capability analysis is an essential step in the new aeroengine design, but containment tests are time-consuming and incur significant costs; thus, developing a short-period and low-cost numerical method is warranted. Using explicit nonlinear dynamic finite element analysis software, the present study numerically investigated the high-speed impact process for simulated blade containment tests which were carried out on high-speed spin testing facility. A number of simulations were conducted using finite element models with different mesh sizes and different values of both the contact penalty factor and the friction coefficient. Detailed comparisons between the experimental and numerical results reveal that the mesh size and the friction coefficient have a considerable impact on the results produced. It is shown that a finer mesh will predict lower containment capability of the case, which is closer to the test data. A larger value of the friction coefficient also predicts lower containment capability. However, the contact penalty factor has little effect on the simulation results if it is large enough to avoid false penetration.

Key words: Aeroengine, Blade containment, Simulation methodology, Mesh size, Contact penalty factor, Friction coefficient
doi:10.1631/jzus.A1100294 **Document code:** A **CLC number:** O347.3; V231.91

1 Introduction

A major hazard in modern jet-powered commercial and military aviations is the failure of a blade of an aeroengine fan, compressor or turbine at very high rotating speeds due to high-cycle fatigue, bird strikes, blade detachment, overheating, material defects, etc., which cannot be avoided even in modern advanced gas turbine engines. Failed rotating components can release high-energy fragments that could perforate engine cowling and damage fuel tanks, hydraulic lines, auxiliary power units, and other accessories, affecting the flying performance in a number of direct and indirect ways and even leading to loss of the airplane and hundreds of passengers.

In accordance with international aviation rules, engine design requires that all blade fragments should be contained within the engine casing structure. Thus, blade containment continues to be an active research area in the aeroengine industry. The containment of failed blades is a complex process, which involves high energy, high-speed interactions of numerous locally and remotely located engine components with nonlinearity, large deformation and transient dynamic behavior. As the rapid development of affordable computer technology with high-speed processors, large memories, and large, fast secondary storage devices, many of the computational mechanics technologies necessary for simulating this behavior have been developed over decades, contributing to the

‡ Corresponding author

* Project supported by the Zhejiang Provincial Natural Science Foundation of China (No. Y1090245), and the Chinese Aviation Propulsion Technology Development Program (No. APTD-11)

integration of these analysis tools within design and analysis groups in industry. This technology transfer has provided methods and software that can be used to improve designs, reduce uncertainties, and increase product safety (Knight *et al.*, 2000). Stallone *et al.* (1983) first studied the transient nonlinear response of a complete aircraft engine system due to the loss of a fan blade based on the component element method. Sarkar and Atluri (1996) investigated the effects of multiple blade interaction on the containment of blade fragments during a rotor failure by comparing with experimental results and numerical computation results using DYNA 3D as the solver. Carney *et al.* (2002) assembled a finite element model of a fan case, a first stage compressor blade assembly, and a rotor on bearings in LS-DYNA to study the global behavior of the blade-out event. Analyses of aeroengine fan blade-out events were also conducted in (Cosme *et al.*, 2002; Shmotin and Gabov; 2006; Heidari *et al.*, 2008; Sinha and Dorbala, 2009; Jain, 2010; He *et al.*, 2012). Xuan and Wu (2006) and Li *et al.* (2009) carried out aeroengine turbine blade and disk containment tests respectively and analyzed them using numerical simulations with LS-DYNA.

However, one of the primary concerns of aircraft structure designers is the accurate simulation of the blade-out event. Reliable simulations of the blade-out event are required to ensure structural integrity as well as to guarantee successful blade-out certification testing. Developing accurate finite element models and analysis strategies for this event has the potential of significantly improving the design, reliability, and safety of engines and primary aircraft structures, especially for commercial transport applications. According to (Zukas and Scheffler, 2000), the causes of disagreement between large-scale code calculations and real problems involving fast, transient loading largely derive from the meshing of the finite element model, the constitutive model accounting for material behavior, and the contact surfaces and material transport accounting for contact-impact situations. The effects of mesh refinement on numerical simulations of uncontained engine debris impact on thin plates were both studied by Knight *et al.* (2000) and Ambur *et al*. (2001). The effects of various factors related to material interfaces in Lagrangian and Eulerian shock-wave-propagation codes were investigated by Scheffler and Zukas (2000). The influences of constitutive relations were conducted in numerical simulations with LS-DYNA by Dey *et al*. (2007). Evaluation of fracture models employed in commercial nonlinear finite element codes was completed by Wierzbicki *et al.* (2005) and Teng and Wierzbicki (2006). Morris and Vignjevic (1997) proposed a method that can provide error control and error bounding methods applicable to the finite element analysis process.

The aim of this work is to develop a blade/case impact numerical simulation method for future use as a part of aeroengine blade containment analysis methodology. Following this brief introduction, the experimental setup and nine blade/case containment tests are presented in Section 2. The only variables studied during testing are the case wall thickness, the blade length and width, and the blade releasing speed. In Section 3, the first test (Test 1) data is simulated with different finite element models using the commercially available explicit dynamic analysis code ANSYS/LS-DYNA to assess the effects of mesh size, contact penalty factor and friction coefficient on numerical simulations, where a numerical method for steel blade/case containment simulation is formed and developed. Then, the developed simulation method is applied to the other eight tests and good agreements are in general obtained between the numerical and test results. Finally, conclusions are made and a simulation methodology for aeroengine blade/case containment is proposed.

2 Experimental setup

Component level containment test using high-speed rotor spin testing facility is an appropriate method to study the behavior of blade/case impact, penetration and perforation. Nine tests were conducted on the ZUST1 high-speed rotor spin tester driven with a new 55-kW DC motor, controlled by a computer automatic testing control system (Fig. 1). A schematic of the test frame is shown in Fig. 2. A plate blade was connected to the rim of the disk with a round pin and was notched at two side edges with the same length forcing it to release within the predicted rotating speed range. The testing procedure was the same as that in (Xuan and Wu, 2006). The materials used in the tests were the Chinese standard 20 steel for

Fig. 1 ZUST1 spin tester with computer automatic control system at the High-Speed Rotating Machinery Laboratory (HiRoMa Lab.) of Zhejiang University, China

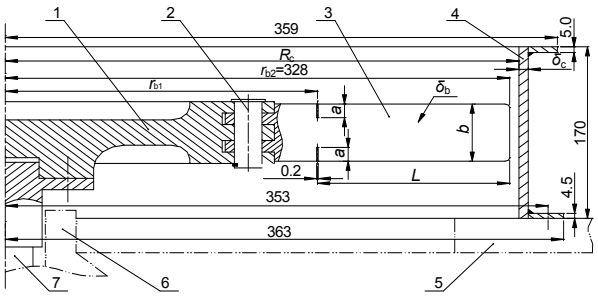

Fig. 2 Sketch of the experimental setup (unit: mm)
1: disk; 2: connecting pin; 3: blade; 4: containment case; 5: testing chamber floor; 6: bearing limit; 7: flexible spindle

the containment case and 45 steel for the released blade (Yu *et al.*, 2012). The dimensions of the test components are listed in Table 1. In Fig. 2 and Table 1, R_c and δ_c are the inner radius and the thickness of the case, respectively; a, L, b, δ_b, m_b, r_{b1} and r_{b2} are the notch depth, length, width, thickness, mass, root radius and tip radius of the released blade, respectively.

A comparison between the predicted and experimental data of the blade releasing speed for each test is given in Table 2. Good agreement between our computational predictions and the test results is obtained within a difference of less than 6.8%. The initial kinetic energies (E_k) of each released blade and the contained or uncontained results are also listed in Table 2.

3 Numerical simulation methodology

Numerical simulations have been increasingly used to improve design and safety, and provide

Table 2 Comparisons of the predicted and experimental blade releasing speeds

Test No.	n_{off} (r/m)		Error (%)	E_k (J)	Result
	Predicted	Experimental			
1	10200	10268	0.67	6263	Uncontained
2	9000	9416	4.62	5220	Uncontained
3	8500	8879	4.46	4644	Uncontained
4	10332	10585	2.45	6218	Contained
5	15000	13981	6.79	12871	Contained
6	9000	9473	5.26	4726	Contained
7	11000	11023	0.21	7499	Contained
8	13400	13389	−0.08	6334	Contained
9	13400	13957	4.16	5686	Contained

n_{off}: released speed

Table 1 Dimensions of the cases and the blades

Test No.	Case		Released blade						
	R_c (mm)	δ_c (mm)	a (mm)	L (mm)	b (mm)	δ_b (mm)	m_b (g)	r_{b1} (mm)	r_{b2} (mm)
1	335	2.2	12.44	140	40	3.6	157.4	188	328
2	334	2.1	14.14	140	40	3.6	157.4	188	328
3	334	1.8	14.80	140	40	3.6	157.4	188	328
4	335	3.0	12.90	125	40	3.6	140.6	203	328
5	334	6.0	7.47	115	50	3.6	161.7	213	328
6	334	2.7	14.90	115	40	3.6	129.4	215	328
7	335	5.0	16.24	105	50	3.6	147.4	223	328
8	335	5.0	18.15	50	50	3.6	70.3	278	328
9	335	5.0	19.43	40	50	3.6	56.2	288	328

insights into details which are very difficult to observe in the testing procedure. In this section, we discuss the development of a numerical simulation methodology suitable for modeling an aeroengine blade-out event. Note that the numerical results depend on the chosen calibration method. Therefore, the first test (Test 1) with the blade uncontained is selected and simulated by ANSYS/LS-DYNA with different finite element models, which include refinements of both the case and released blade, variations of the contact penalty factor and the friction coefficient values, to assess the influences of these factors on modeling, and hence form a suitable simulation method for aeroengine blade containment analysis.

3.1 Computational model

The detailed data of the released blade and case in Test 1 are listed in Table 1. The blade was released at a rotation speed of 10268 r/min. It bent plastically into a "U" shape and perforated the case with a large hole as shown in Fig. 3. The deformed shape of the case with respect to the original shape taken in the mid-section plane of the blade is shown in Fig. 4. Two major impact regions were observed on the case (Fig. 3) and are shown as "1st" and "2nd" for the first and the second impact regions, respectively in Fig. 4. Compared with the second impact region, the first one is much smaller. Only a shallow crater is formed and no fracture appears. But in the second impact region, the crater is large and tearing failure occurs along the circumferential direction beneath the two side edges of the moving blade. To describe the plastic deformation on the case, we use the following parameters (Fig. 4): the circumferential angle of the whole plastic deformation area, θ_p; the maximum depths in the two impact regions, h_1 and h_2; the circumferential angle between the two maximum depths, θ_{12}; and the circumferential angle of the tearing failure area in the second impact region, θ_t. The measuring results for these parameters in Test 1 are: h_1= 7.0 mm, h_2=25.0 mm, θ_p=56.4°, θ_{12}=40.5°, and θ_t=16.3°.

The LS-DYNA finite element computational model was established with an initially released blade fragment and a containment case, as shown in Fig. 5. Both the case and the blade were modeled using eight-node solid elements with one point integration and stiffness based hourglass control, where the hourglass coefficient was set to a default value of 0.1. Eight-node solid elements can observe the failure mode through the thickness which cannot be easily obtained with other element types, such as the shell element. To obviate the need for cumbersome elements, and thus decrease the computer resources demanded for each computation, mesh refinement was adopted in the impact zone of the case and in the released blade. The impact zone of the case, defined as a quarter in the circumferential direction starting from the initial angular position of the blade when it is released along the direction of rotor rotation and a third in the axial direction, is shown in Fig. 5. The released

Fig. 3 Perforated case (left) and the bended blade (right) of Test 1

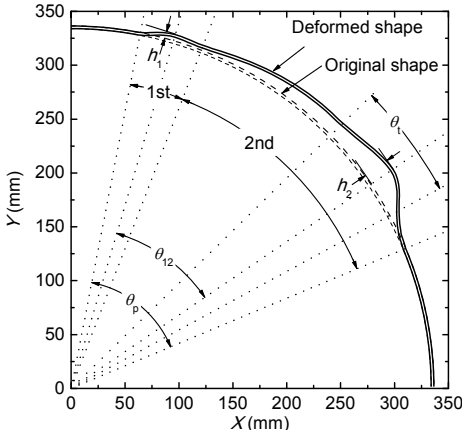

Fig. 4 Posttest deformation of the case taken in the mid-section plane of the blade

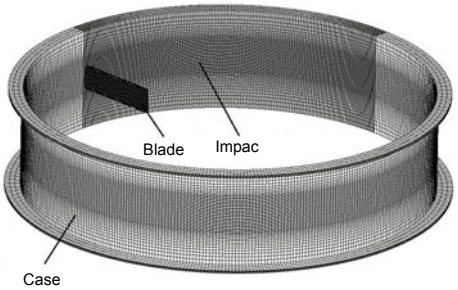

Fig. 5 Initial computational model configuration

blade had a uniform mesh for its whole bending deformation during the impact. In Fig. 5, the relative dark bar is indicative of the level of mesh refinement in that region. In the present study, crack propagation time was assumed to be zero, thus the blade fragment was separated from the blade stem at the start of the analysis. In accordance with the setup and results of Test 1, the nodes within the bottom flange surface of the casing were constrained and the blade was given an initial angular velocity ω=1075 rad/s.

Contact algorithms have always been an important capability in impact simulation software. Contact may occur between two or more impacting bodies, or along surfaces of a single body undergoing large deformation. In this work, the contact algorithm between the blade and the case was single surface eroding (ESS), which can describe the contact between the casing and the blade as well as the blade contact with itself. All the outer surfaces were considered as the contact surface. A contact penalty factor was defined to control the contact problem to a certain extent. This factor is related to the contact force on the structure and the amount of penetration occurring for the bodies in contact. The contact force changes with the value of this factor proportionally for a given penetration distance and thereby reduces the non-physical energy related to this interaction. Ideally, the value of this factor should be as large as possible to prevent penetration; however, it needs to be small enough to guarantee numerical stability. The sliding interface with friction and separation approach was used to model the impact event between the released blade and the case, and only a constant friction coefficient was used to describe it.

The LS-DYNA code permits automatic examination of the finite element mesh and material properties to determine an appropriate time step size for numerical stability. This time step size is then automatically adjusted throughout the transient analysis based on the deformation and stress state of each structural element.

3.2 Constitutive relation

The blade tip velocity in Test 1 reached 353 m/s as the rotating speed was 10268 r/min. The released blade impact on the containment case involves viscoplasticity, large deformation, and transient dynamic behavior subject to extreme loading conditions, so it is necessary to establish a reliable constitutive relation and fracture criteria as a function of large strain, high strain rate, softening temperature, varying stress state, and history of loading in addition to damage accumulation and various failure modes in numerical simulations. According to (Wierzbicki *et al.*, 2005; Teng and Wierzbicki, 2006; Dey *et al.*, 2007), the Johnson-Cook (J-C) constitutive relation and fracture criterion are a good choice for this particular engineering problem and can be applied to the materials of both the blade and the case.

The J-C constitutive relation proposed by Johnson and Cook (1983) has been frequently used, which can be expressed as

$$\sigma_{\mathrm{e}} = [A + B(\varepsilon_{\mathrm{e}}^{\mathrm{p}})^{n}][1 + C\ln\dot{\varepsilon}^{*}][1 - T^{*m}], \quad (1)$$

where A, B, C, n and m are material constants, σ_{e} is the equivalent von Mises stress, $\varepsilon_{\mathrm{e}}^{\mathrm{p}}$ is the equivalent plastic strain, $\dot{\varepsilon}^{*} = \dot{\varepsilon}_{\mathrm{e}}^{\mathrm{p}} / \dot{\varepsilon}_{0}$ is a dimensionless strain rate, and $\dot{\varepsilon}_{0}$ is a user-defined reference strain rate; $T^{*}=(T-T_0)/(T_{\mathrm{melt}}-T_0)$ is the homologous temperature, where T is the absolute temperature, T_0 is the room temperature, and T_{melt} is the melting temperature of the material.

The J-C fracture criterion (Johnson and Cook, 1985) is based on damage evolution, while the damage D of a material element is expressed as

$$D = \sum(\Delta\varepsilon_{\mathrm{e}}^{\mathrm{p}} / \varepsilon_{\mathrm{f}}), \quad (2)$$

where $\Delta\varepsilon_{\mathrm{e}}^{\mathrm{p}}$ is the increment of equivalent plastic strain that occurs during an integration cycle and ε_{f} is the fracture strain. Failure is represented by element erosion when D equals unity. Fracture strain depends on stress triaxiality, strain rate and temperature, and is given by

$$\varepsilon_{\mathrm{f}} = \left(D_1 + D_2 \mathrm{e}^{D_3\sigma^{*}}\right)\left(1 + D_4 \ln\dot{\varepsilon}^{*}\right)\left(1 + D_5 T^{*}\right), \quad (3)$$

where D_1–D_5 are material constants, $\sigma^{*}=p/\sigma_{\mathrm{e}}=-R_{\sigma}$, R_{σ} is the stress triaxiality ratio, and p is the pressure.

To describe the pressure-volume (p-V) relationship, the Gruneisen equation of state with cubic shock velocity-particle velocity (v_{s}-v_{p}) relationship

was used to define pressure depending on whether the material is compressed or expanded. For compressed materials, it is given by (Hallquist, 2006)

$$p=\frac{\rho_0 C_s^2\mu\left[1+\left(1-\frac{\gamma_0}{2}\right)\mu-\frac{\alpha}{2}\mu^2\right]}{\left[1-(S_1-1)\mu-S_2\frac{\mu^2}{\mu+1}-S_3\frac{\mu^3}{(\mu+1)^2}\right]}+(\gamma_0+\alpha\mu)E, \tag{4}$$

and for expanded materials, it is expressed as

$$p=\rho_0 C_s^2\mu+(\gamma_0+\alpha\mu)E, \tag{5}$$

where C_s is the intercept of the v_s-v_p curve; S_1, S_2 and S_3 are the coefficients of the slopes of the v_s-v_p curves, γ_0 is the Gruneisen gamma, α is the first-order volume correction to γ_0, ρ_0 is the initial density, E is the internal energy, and $\mu=1/V-1$.

The material constants for the 20 steel and 45 steel in (Chen *et al.*, 2005; 2007; Fan *et al.*, 2006) were used in this study, and which are compiled in Table 3.

3.3 Impact zone refinement of the case

It is well known that mesh density is a prime consideration in the determination of model accuracy and computation time for penetration simulation. The accuracy of the solution can increase with a higher mesh density. However, this usually results in more computer resources and a longer computational run time. Therefore, a local mesh density study was performed in the impact zone of the case to achieve the balance of accuracy and run time. This section assesses the spatial discretization needs in the impact zone of the case. Finite element refinement studies were performed wherein different levels of mesh refinement were used for the impact zone of the case while all the other conditions being kept unchanged. In these studies, the finite element model of the released blade was kept identical and had a uniform mesh with its in-plane element size of 0.9 mm in the L direction and 1.0 mm in the b direction (Fig. 2), and with four elements through the thickness. There were a total of 25840 eight-node solid elements in the released blade. Two types of mesh refinement were considered in the impact zone of the case, including different in-plane spatial discretizations (Type A) and through-the-thickness mesh discretizations (Type B). A summary of the finite element models for the case used in various spatial discretization studies is given in Table 4. In the notation "Ci-j", "i" denotes the in-plane mesh and "j" denotes the number of elements through the thickness. In the following tables, the model with "*" in the notation is used as a reference.

Table 3 Material constants of 20 and 45 steels for the J-C constitutive relation and fracture criterion

Material	Physical constant						J-C constitutive relation constant					
	E (GPa)	v	ρ (kg/m^3)	T_{melt} (K)	T_0 (K)	C_ρ (J/(kg·K))	$\dot{\varepsilon}_0$ (s^{-1})	A (MPa)	B (MPa)	C	n	m
20 steel	200	0.3	7.82×10^3	1783	293	465	1	258	329	0.045	0.24	1.00
45 steel	200	0.3	7.82×10^3	1783	293	465	1	630	822	0.064	0.47	1.06
Material	Gruneisen equation of state constant						J-C fracture criterion constant					
	C_s (m/s)	S_1	S_2	S_3	γ_0	α	D_1	D_2	D_3	D_4	D_5	
20 steel	4569	1.49	0	0	2.17	0.46	0.35	0.25	4.80	0.005	−0.84	
45 steel	4569	1.49	0	0	2.17	0.46	0.10	0.76	1.57	0.005	−0.84	

C_ρ is the specific heat capacity of the material

Table 4 Summary of the finite element models for impact zone refinement of the case

Case model		In-plane element size of the impact zone (circumferential direction×axial direction)	Element size through the thickness	Element number of the case model
Type A	C1-3	1.82 mm×1.81 mm	0.833 mm	89796
	C2-3	1.20 mm×1.20 mm	0.833 mm	129340
	*C3-3	0.90 mm×0.90 mm	0.833 mm	179640
	C4-3	0.72 mm×0.72 mm	0.833 mm	239172
Type B	C3-2	0.90 mm×0.90 mm	1.250 mm	118046
	*C3-3	0.90 mm×0.90 mm	0.833 mm	179640
	C3-4	0.90 mm×0.90 mm	0.625 mm	236092

The contact penalty factor, the friction coefficient and the total simulation time were kept at 0.1, 0.15 and 2.5 ms, respectively. Computations were carried out on a Linux workstation, which has two Intel Xeon 5420 CPUs with 2500 MHz main frequency, and a bus frequency of 1333 MHz, RAM 8 GB, two SAS hard disks of total 272-GB storage space.

Table 6 Comparison of the deformation and failure on the case between the test and numerical results

Test/Model No.	h_1 (mm)	h_2 (mm)	θ_p (°)	θ_{12} (°)	θ_t (°)
Test 1	7.0	25.0	56.4	40.5	16.3
C1-3	8.6	19.7	53.8	35.8	0
C2-3	7.8	23.3	52.3	39.5	13.4
*C3-3	6.9	24.7	55.6	40.0	15.6
C4-3	6.4	25.3	54.0	39.8	16.1
C3-2	8.4	22.2	57.7	40.9	15.0
C3-4	5.3	25.0	54.8	39.0	16.5

The finite element studies are based on the assessment of the time variations of the kinetic and strain energies of both the released blade and the case, the contact force, the final deformed shape of the released blade, and the craters and the tearing failure hole on the case. Numerical results of the above six different models are listed in Tables 5 and 6, and shown in Fig. 6, where KE_{bi}, KE_{br} and IE_b are the initial kinetic energy, the residual kinetic energy and

Table 5 Simulation results of the six different models for impact zone refinement of the case

Test/model No.	Kinetic energy (kJ)		Strain energy (kJ)		Perforation result of the case
	KE_{bi}	KE_{br}	IE_c	IE_b	
Test 1 (test data)	6.263	–	–	–	Circumferential tearing
C1-3	6.263	0.473	3.459	1.135	Deformation only
C2-3	6.263	0.209	3.488	1.137	Circumferential tearing
*C3-3	6.263	0.224	3.447	1.123	Circumferential tearing
C4-3	6.263	0.244	3.450	1.101	Circumferential tearing
C3-2	6.263	0.157	3.453	1.164	Circumferential tearing
C3-4	6.263	0.249	3.450	1.161	Circumferential tearing

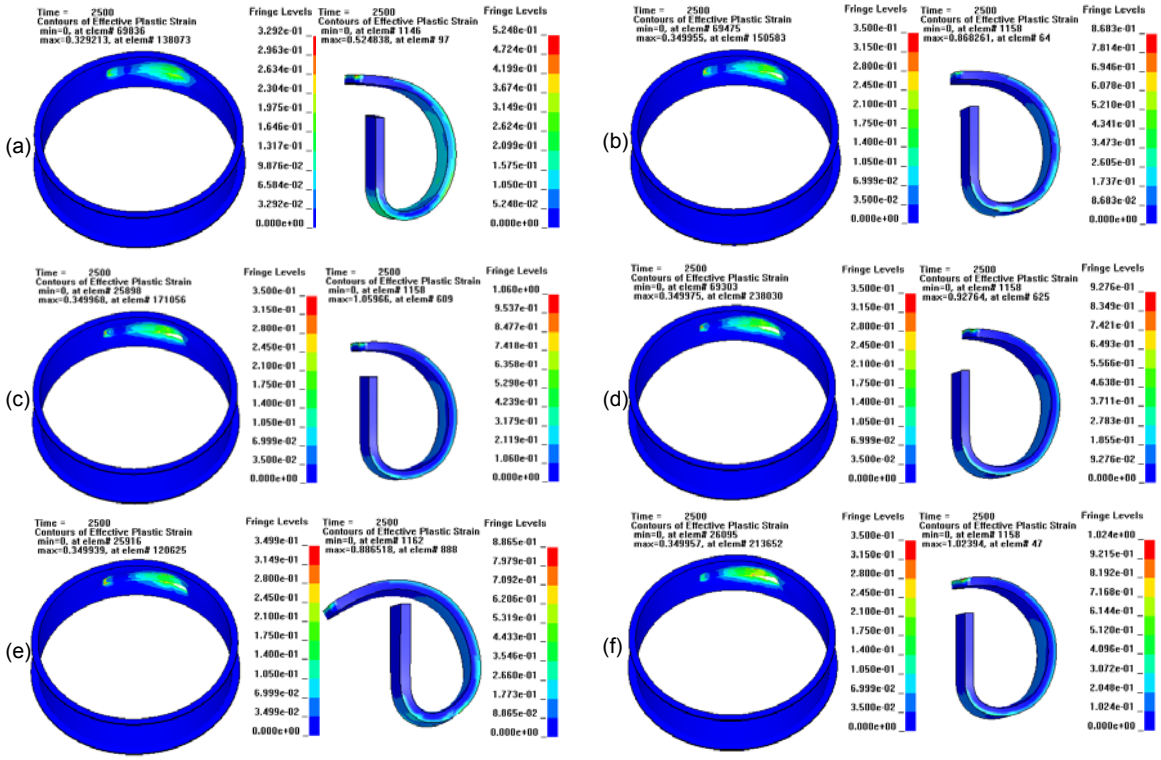

Fig. 6 Simulation results of six different finite element models (fringe level of plastic strain)
(a) C1-3 model; (b) C2-3 model; (c) C3-3 model; (d) C4-3 model; (e) C3-2 model; (f) C3-4 model

strain energy of the blade, respectively, and IE_c is the final strain energy of the case. There is much energy loss due to failed elements eroding, hourglass control, friction between sliding surfaces and kinetic energy dissipation on the bottom flange of the case that is fixed to the spin tester through the connection bolts.

Similar results of the post-impact energies of the blade and case are obtained with six different finite element discretizations. The KE_{br}, IE_b and IE_c contain errors within 5%, 1% and 0.7% of the initial kinetic energy of the blade, respectively. However, the plastic deformations of both the blade and the case have obvious differences (Fig. 6 and Table 6). The case is not perforated in C1-3, and the blade bends too much in C3-2 as a result of using a relatively coarse mesh through the thickness. With a more refined mesh for the case impact zone, the depth of the first crater (h_1) on the case is smaller, but the depth of the second crater (h_2) and the circumferential angle of the tearing area (θ_t) are larger. Overall, the plastic deformations of both the blade and the case predicted by a finer mesh for the case are closer to the experimental results. Comparisons of several selected parameters for different meshes are shown in Figs. 7–11.

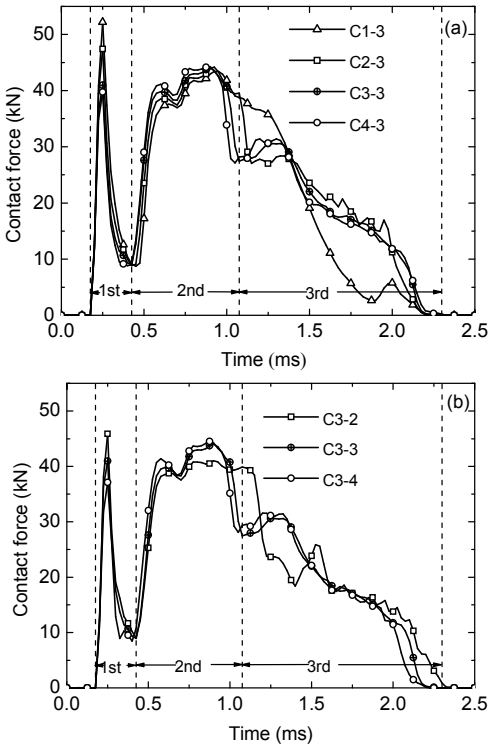

Fig. 7 Variations of contact force between the case and the blade during impact process
(a) Type A; (b) Type B

Fig. 7 shows the variations of the contact force between the case and the blade during the whole containment process. There are three major impacts found according to the curves, and all the selected parameters for the different meshes mentioned in the following paragraphs are divided into three stages using C3-3 (or B2) as a reference, which are named as 1st, 2nd and 3rd for the first, the second and the third stage, respectively. As the shortest duration, the first stage begins at 0.175 ms and lasts for about 0.250 ms with a peak value of 41.0 kN occurring at 0.250 ms. Then the second stage follows, with a higher peak value of 44.0 kN and a longer duration time of about 0.650 ms, doing the most harmful damage to the case because of its high tendency of initializing circumferential tearing through the whole thickness of the case. The third stage starts from 1.075 ms and has the longest duration time of about 1.225 ms.

It is found that the models with finer mesh have lower peak values of contact force during the first stage and higher peak values during the following stages. It argues that with a finer mesh in the impact zone the case is easier to deform; hence, the contact force is lower during the first stage and more kinetic energy of the blade is retained in the following stages, which causes a higher level of contact force during the later stages. The mesh of C1-3 is so coarse that no element fails or erodes, and only two stages are predicted by this model. There are elements eroded for C2-3 but only a short length of circumferential tearing through the whole thickness of the case is predicted. Longer tearing lengths are predicted in C3-3, C4-3, C3-2 and C3-4, closer to the tearing length observed in Test 1. The time variation curves of contact force for C3-3, C4-3 and C3-4 tend to converge.

Variations of the strain energy of the case are given and compared in Fig. 8. After the beginning of the impact process, the strain energies of the case for the six models begin to differ from each other, and the differences among them develop to a maximum at the end of the first stage though these differences are small. The model with a more refined mesh predicted less strain energy absorbed by the case as a result of a lower level of contact force exerted on the case as shown in Fig. 7. When the second stage starts, the

differences decrease, then almost disappear, and finally increase in the opposite direction with less strain energy for a less refined mesh. The case gains more than 60% of its total strain energy during the second stage and keeps a fast strain energy growth throughout the second stage. It is considered that the end of the second stage is a critical moment because the most serious damage to the case will take place at this point. The case is extruded with a maximum depth at this critical point. Since a less refined model predicts less strain energy at the end of the second stage, this model can absorb more strain energy and permit further deformation, thus owns an enhanced containment capacity. It argues that if a less refined model predicts a blade contained result, the convergent result with a highly refined mesh might be uncontained; on the other hand, if a less refined model predicts a blade uncontained result, the convergent result must be uncontained. Following the second stage, the third stage arrives with a relative weak interaction between the case and blade. The strain energy growth slows down and the deformation continues to evolve. The maximum differences of the strain energies for different finite element discretizations appearing during the first stage can be explained by forceful contact and intense localized plastic deformation, thus a very refined mesh should be used in the first impact region of the case to capture this phenomenon. The strain energies for cases C3-3, C4-3 and C3-4 are close and are considered to be convergent.

Comparisons of the kinetic and the strain energies of the released blade for the six models are given in Figs. 9 and 10. The kinetic energy level for a less refined model is lower during the first and third stages, but is higher during the second stage in most cases, except for C1-3 since it cannot predict the circumferential tearing. Except for C1-3 and C3-2, the differences between different meshes increase during the first stage and decrease during the third stage monotonically, but for the second stage, the differences between them first decrease, then increase, and finally decrease (Fig. 9). The element size is too large to describe the in-plane tearing for C1-3 and to capture the deformation through the thickness for C3-2.

The strain energy level of the blade for the more refined model is higher during the first and second stages and lower during the third stage (Fig. 10). The front half of the blade prior to contact with the case deforms more seriously and the back half bends less

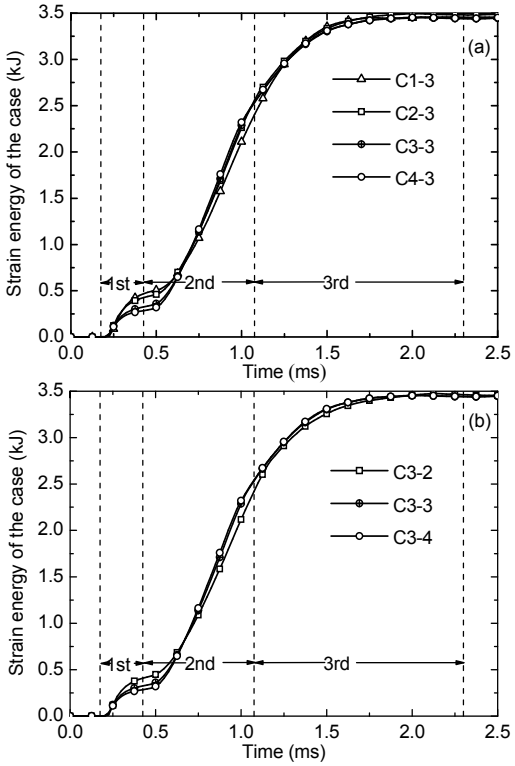

Fig. 8 Strain energies of the case for different meshes
(a) Type A; (b) Type B

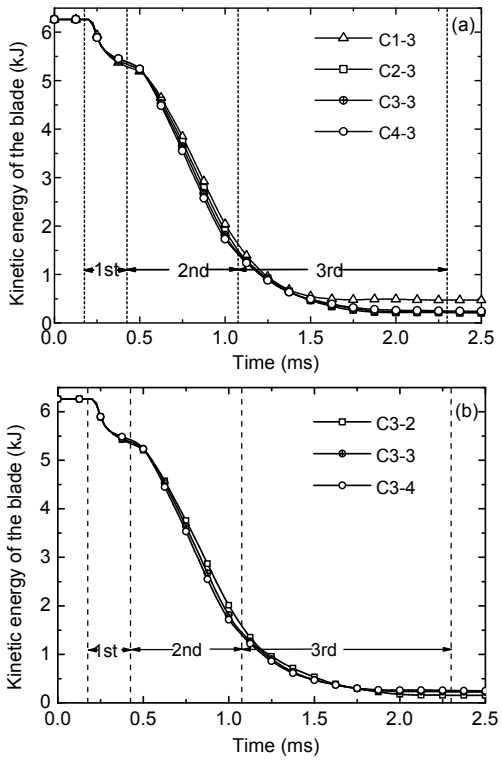

Fig. 9 Kinetic energies of the blade for different meshes
(a) Type A; (b) Type B

as shown in Fig. 6. It indicates that for a more refined model of the case, the deformation is more localized.

While the second stage is a critical period in which initial perforation of the case will happen, less kinetic energy of the blade is left after the first stage and more kinetic energy remains during the second stage for the less refined model. During the second stage, there is less kinetic energy loss which will be mainly transformed into strain energy of the case, so that the safety of the case is reinforced and its containment capacity is enhanced. The differences in the strain and the kinetic energies for the different finite element models are minor but the differences in the deformations of the case shaped by the blade are obvious.

Six trajectories of the centroid of the released blade in the *XY* plane (a plane that is perpendicular to the rotation axis) for the six models are given in Fig. 11. Before impacting on the case, the trajectories of the centroid of the blades are straight lines as no counter force is exerted on the blade, and the six curves overlap. After then, the trajectories begin to bend and get closer to the inner wall of the case as a result of the impact interactions between the blade and the case. The centroid of the blade is closer to the inner wall of the case for more refined mesh models. It is because with a smaller mesh size, whether in-plane or through the thickness, the impact zone of the case is easier to deform and capture the local deformation and is also more able to allow the blade to move forward. The angular ranges for the three stages are from 10.7° to 24.3°, 24.3° to 49.0°, and 49.0° to 60.0°, respectively.

Although the differences in kinetic and strain energies between the six models are small, the deformations of both the case and the blade exhibit significant differences. It is concluded that a model with more local refined mesh in the impact zone can better capture the localized elastic-plastic deformation of the case. In summary, the refinement of element size with 0.9 mm×0.9 mm in-plane and three elements through the thickness in the impact zone of the case are refined enough to obtain convergent results consistent with the test data.

3.4 Blade refinement

In this section, another refined method is studied in detail with different finite element discretizations

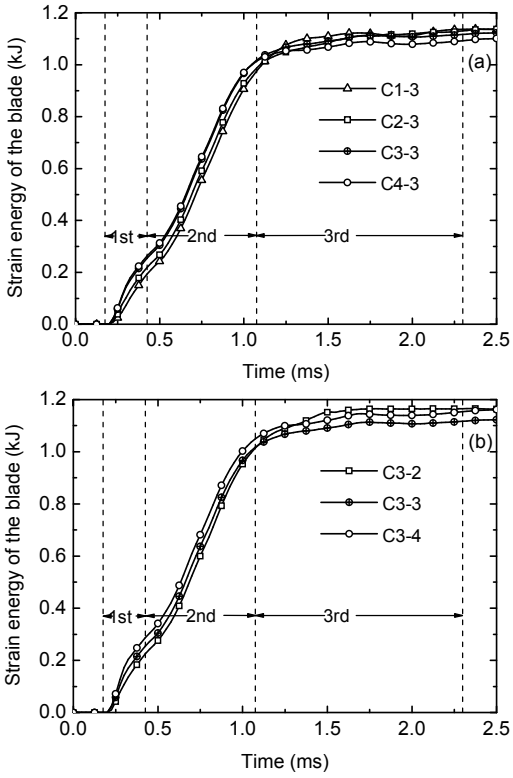

Fig. 10 Strain energies of the blade for different meshes
(a) Type A; (b) Type B

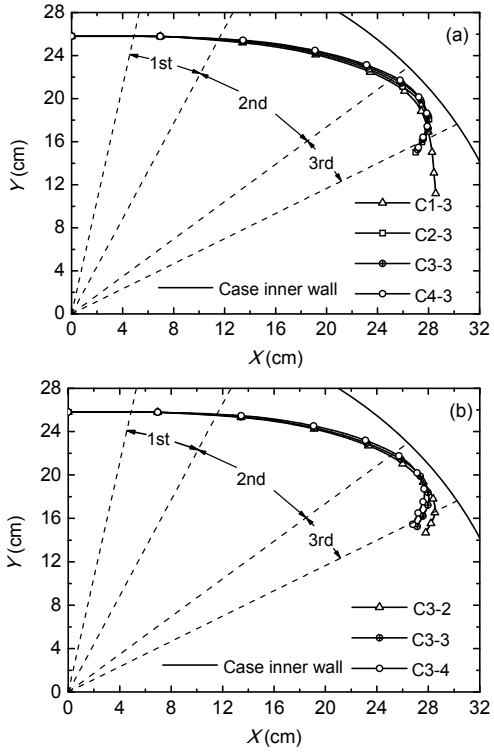

Fig. 11 Trajectories of the centroid of the blade in the *XY* plane for different modes
(a) Type A; (b) Type B

for the released blade. According to Section 3.3, C3-3 for the case tends to converge for all the parameters selected and is considered to be sufficiently refined. Therefore, the finite element mesh of the case in C3-3 is used as an unchanged condition. Moreover, all the other parameters are kept the same as shown in Section 3.3. A summary of the finite element models for the blade with various spatial discretizations is given in Table 7. In the notation "Bi" for the blade models of type A, element size is approximately equal in the three directions and "i" denotes the mesh size; while in the notation "B2-*" for the blade models of type B, the element size in the "*" direction is twice the size in the other two directions. The mesh for the blade of the model B2 is the same as that for the blade model in Section 3.3.

The results of the transfer, transformation and dissipation of the initial kinetic energy of the released blade are listed in Table 8. Deviations of the results of KE_{br}, IE_c and IE_b for the six computational models are all within 3.2%, 6.1% and 3.2% normalized by the initial kinetic energy of the blade (KE_{bi}), respectively. The case is perforated with circumferential tearing along the blade rotation direction for all the six models. Mesh size of the cubic elements for the blade has a significant effect on energy transformation. More kinetic energy is transformed into strain energy of the case with a more refined mesh of the blade.

The shapes of the perforated hole on the case and the bending deformations of the released blade are shown in Fig. 12. The deformation data of the impact regions on the case are given in Table 9. As the mesh of the case is identical, the effects of the blade mesh size on the tearing failure of the case are not significant. But with a coarse mesh for the blade model, smaller depths of the craters on the case and more global bending deformation of the blade are predicted. It is observed that mesh size in the width direction of the blade has a minimal effect on the final deformation of the blade.

Fig. 13 shows the variations of the contact force between the case and blade during impact for the six models. Likewise, three stages are predicted by all the models. During the first stage, the differences in the contact area between the models are large as a result of line contact. A more refined mesh for the blade predicts smaller contact area, and thus predicts higher peak value of the contact force. Besides, increasing the element size in the blade's width direction, such as in the B2-W model, only has a small effect on the contact force. The contact forces predicted by the B2 and B3 models are almost the same. Therefore, it is concluded that the B2 model is refined enough for prediction of the contact force.

Table 7 Summery of the finite element models for the blade with different meshes

Blade model		Element size** (mm×mm×mm)	Total elements of the blade
Type A	B1	1.78×1.79×1.80	3630
	*B2	0.90×1.00×0.90	25840
	B3	0.60×0.61×0.60	95772
Type B	B2-L	1.80×1.00×0.90	13088
	B2-W	0.90×2.00×0.90	12920
	B2-T	0.90×1.00×1.80	12920

** length×width×thickness

Table 9 Comparison of the deformation and the failure on the case between the test and the numerical results

Test/Model No.	h_1 (mm)	h_2 (mm)	θ_p (°)	θ_{12} (°)	θ_t (°)
Test 1	7.0	25.0	56.4	40.5	16.3
B1	3.7	22.8	53.9	39.2	15.7
*B2	6.9	24.7	55.6	40.0	15.6
B3	8.3	25.3	53.9	38.9	15.3
B2-L	4.0	25.3	52.9	38.1	15.0
B2-W	4.9	25.1	53.2	38.9	15.0
B2-T	8.9	21.1	56.3	40.7	13.9

Table 8 Simulation results of the six models for the blade

Test/Model No.	Kinetic energy (kJ)		Strain energy (kJ)		Perforation result of the case
	KE_{bi} (kJ)	KE_{br}	IE_c (kJ)	IE_b	
Test 1 (test data)	6.263	–	–	–	Circumferential tearing
B1	6.263	0.139	3.158	1.254	Circumferential tearing
*B2	6.263	0.224	3.447	1.123	Circumferential tearing
B3	6.263	0.328	3.540	1.052	Circumferential tearing
B2-L	6.263	0.129	3.213	1.205	Circumferential tearing
B2-W	6.263	0.269	3.397	1.156	Circumferential tearing
B2-T	6.263	0.170	3.406	1.182	Circumferential tearing

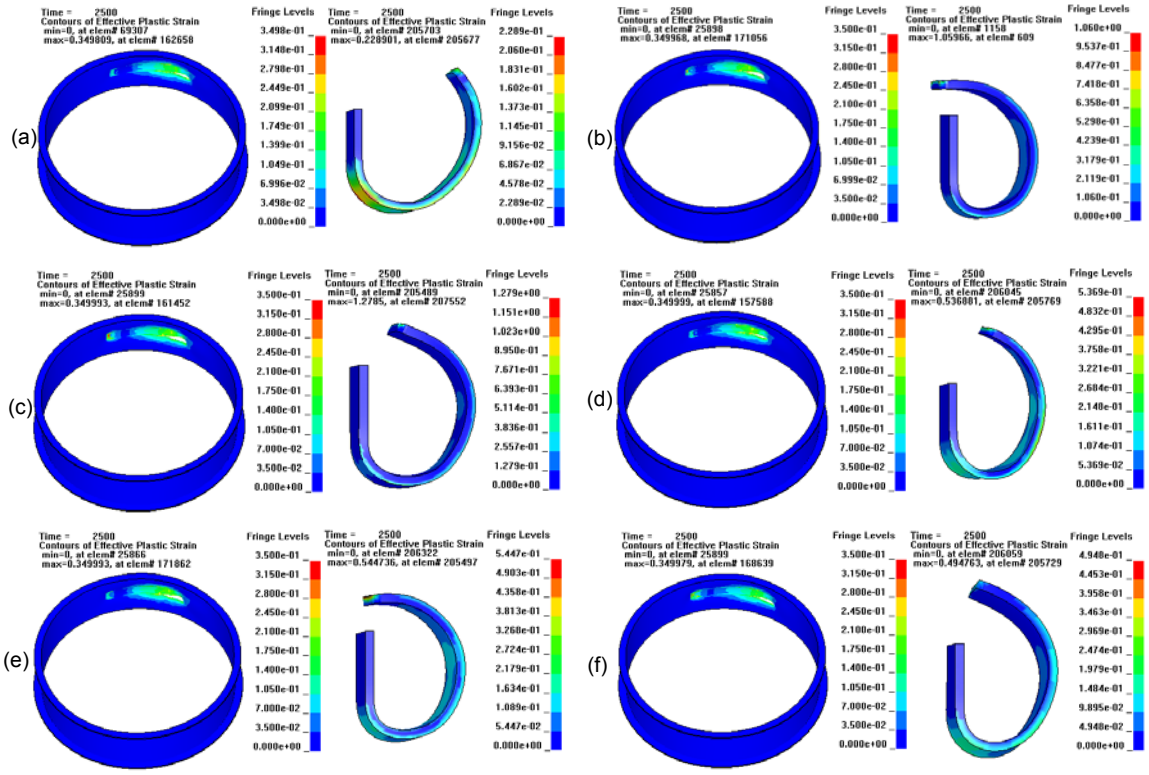

Fig. 12 Simulation results for the six models (fringe level of plastic strain)
(a) B1 model; (b) B2 model; (c) B3 model; (d) B2-L model; (e) B2-W model; (f) B2-T model

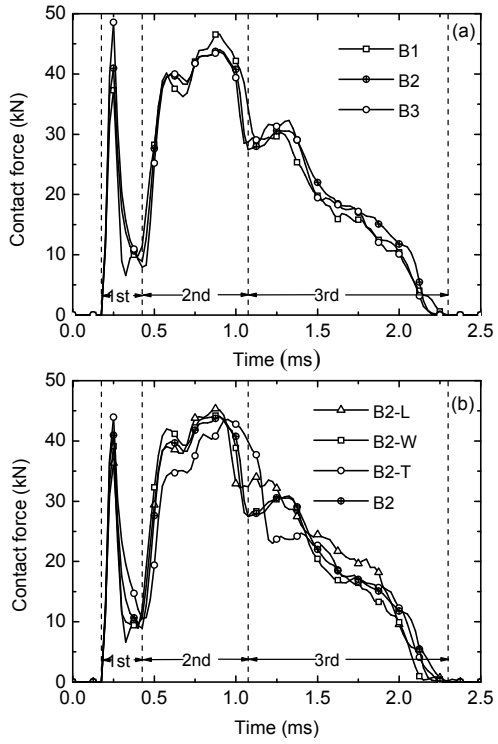

Fig. 13 Contact force between the case and the blade for the six models
(a) Type A; (b) Type B

Fig. 14 shows the variations of the strain energy of the case for the six models. The cubic element size has a significant effect on energy transformation. The strain energy curves have large deviations from each other at the end of the first and third stages. The amount of the strain energy absorbed by the case during the second stage in the B3 model is approximately equal to that in the B2 model and larger than that in the B1 model. It is found that the model with more refined cubic elements predicts more strain energy of the case, so the predicted containment capacity of the case is weakened compared with the less refined model. The strain energy curve of the B2-W model is closer to that of the B2 model than the other two models in Type B. Similarly, increasing the element size in the width direction of the blade has the smallest effect on the strain energy of the case.

Fig. 15 shows the variations of the kinetic energy of the released blade. The kinetic energy curves are very close to each other and almost overlap during the first and second stages, but obvious differences occur and develop to a maximum during the third stage. Less residual kinetic energy is predicted with a less

refined model. Kinetic energy variation in the B2-W model is closer to that in the B2 model.

Fig. 16 shows the variations of the strain energy of the released blade. The model with a more refined mesh predicts less strain energy absorbed by the blade during the whole impact process except for the B2-T model. It is considered that the model with a less refined mesh cannot capture localized elastoplastic deformation well, but predicts more strain energy absorbed through global bending of the blade. Only two elements through the thickness of the blade are used for the B2-T model and this model cannot describe the bending behavior of the blade through the thickness accurately, so the strain energy of the blade, and other parameters discussed above for the B2-T model deviate largely from the other models.

The moving trajectories of the centroid of the released blade in the *XY* plane for the six different models are shown in Fig. 17. The centroid of the blade is closer to the inner wall of the case for less refined models. The differences between the centroid of the blade predicted by the B2-L and B2 models are large. We can conclude that the element size in the length direction has a significant effect on the

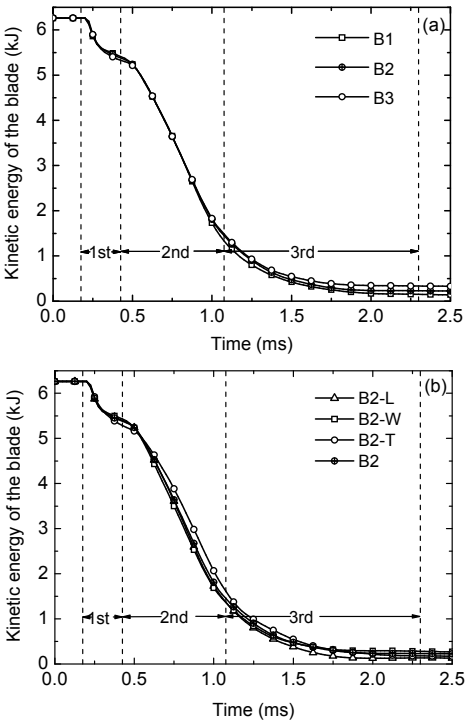

Fig. 15 Kinetic energy of the blade for different blade mesh models
(a) Type A; (b) Type B

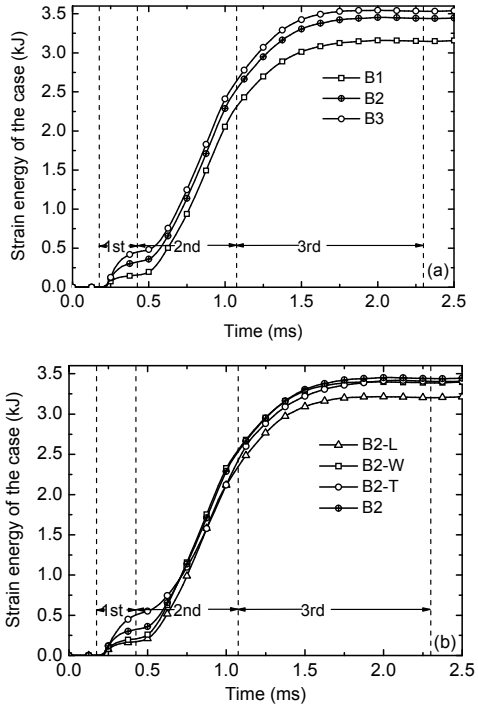

Fig. 14 Strain energy of the case for the six models
(a) Type A; (b) Type B

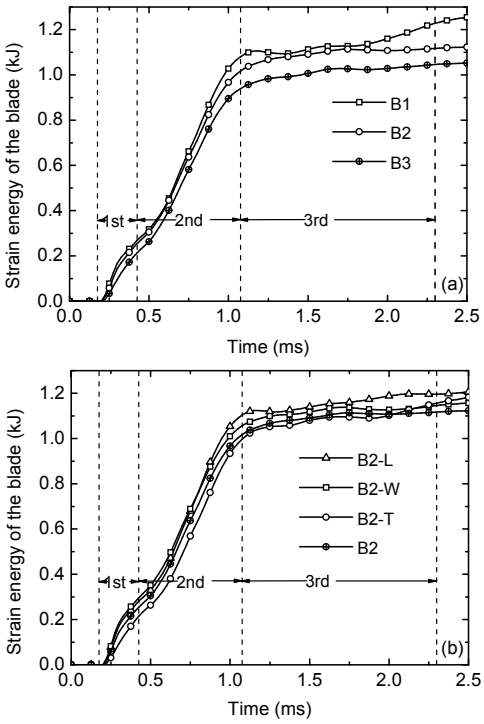

Fig. 16 Strain energy of the blade for different blade mesh models
(a) Type A; (b) Type B

trajectory of the centroid of the blade. The simulation results predicted by the B2, B3, and B2-W models are close, showing that the influence of element size on the blade width direction is insignificant.

In summary, the more refined mesh for the released blade better captures the localized bending pattern, predicts less strain energy of the blade and more strain energy of the case. The element size in the blade width direction has a minimum influence on the simulation results because the entire width of the blade contacts the inner wall of the case in the whole containment process. It argues that the element size for the released blade is refined enough when it equals to that for the impact zone of the case.

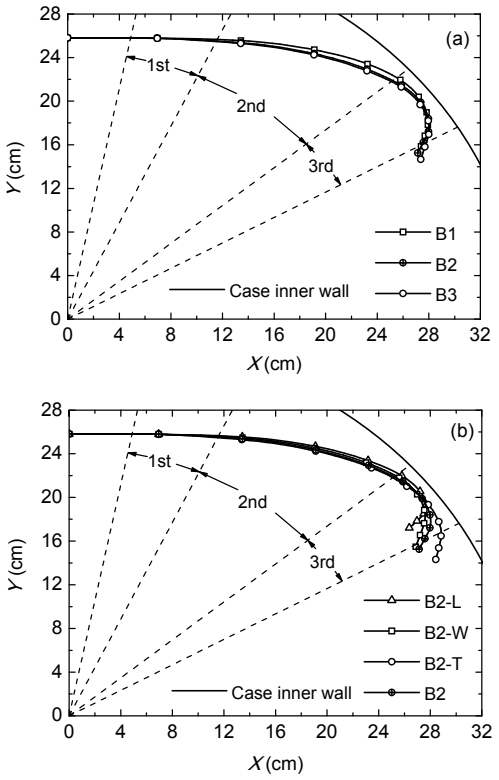

Fig. 17 Trajectories of the centroid of the released blade in the *XY* plane for the six models
(a) Type A; (b) Type B

3.5 Effect of contact penalty factor

There are several contact-related parameters in LS-DYNA that can be used to improve the description of the contact behavior. To study the effects of contact penalty factor used on the aeroengine blade containment simulation, different values of the contact penalty factor were set for the same finite element model. The C3-3 and B2 models were found to be mesh refined enough both for the case discussed in Section 3.3 and for the released blade discussed in Section 3.4. Therefore, the C3-3 mesh patterns were used for the case and the B2 model was used for the blade to conduct this study. The contact penalty factors were set to 0.01, 0.1, 0.5, and 5 in four different simulations. The value of the friction coefficient was kept at 0.15. The results for the simulations with different values of the contact penalty factor are listed in Table 10 and shown in Fig. 18.

The time variations of selected parameters for different contact penalty factor values are compared and given in Figs. 19–23. With a small value of 0.01, the contact force, kinetic energy loss of the blade and strain energies absorbed by the blade and case are very small, and the blade penetrates the case without any damage to the case (Fig.18a). Increasing the values of the contact penalty factor from 0.1 to 5, the time variations of all the selected parameters are close and almost overlap each other.

It indicates that false penetration will be predicted if the contact penalty factor is set too small. The numerical results tend to converge when the contact penalty factor is set large enough. According to the LS-DYNA Theory Manual (Hallquist, 2006), the contact penalty factor should not be set too large else the Courant stability criteria would be violated. If this factor is set too large, numerical instabilities may be caused unless the time step size is reduced to a very small value, which will waste a lot of computing time. As the default value of 0.1 generally works well for contact between similarly refined meshes of

Table 10 Simulation results for different contact penalty factor values

Value of penalty factor	Kinetic energy (kJ)		Strain energy (kJ)		Perforation result of the case
	KE_{bi}	KE_{br}	IE_c	IE_b	
0.01	6.263	6.054	0.034	0.015	Slight deformations
0.1	6.263	0.224	3.447	1.123	Circumferential tearing
0.5	6.263	0.217	3.417	1.141	Circumferential tearing
5	6.263	0.210	3.435	1.120	Circumferential tearing

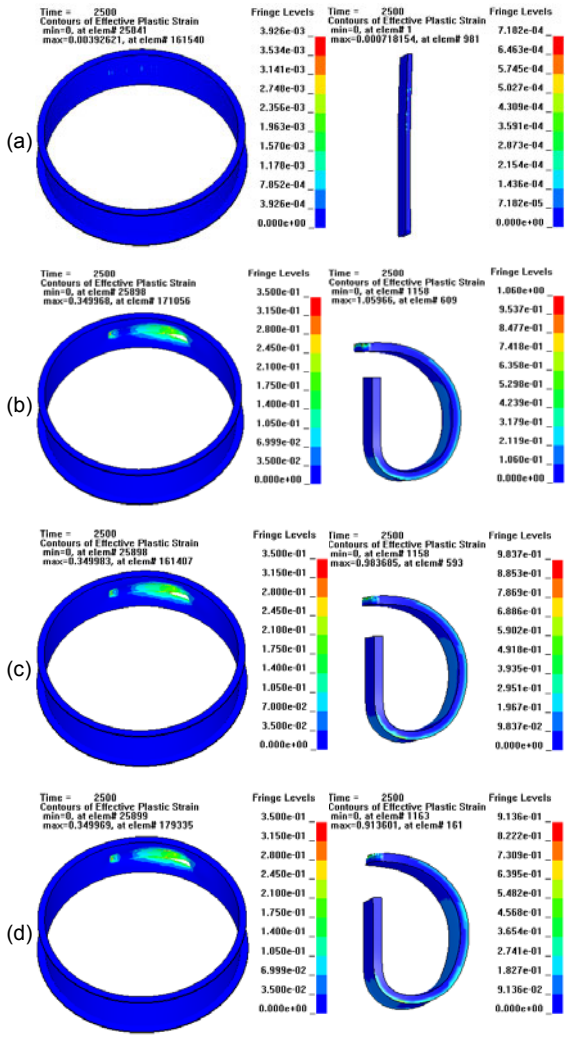

Fig. 18 Simulation results for different contact penalty factor values of 0.01 (a), 0.1 (b), 0.5 (c) and 5 (d) (Fringe level of plastic strain)

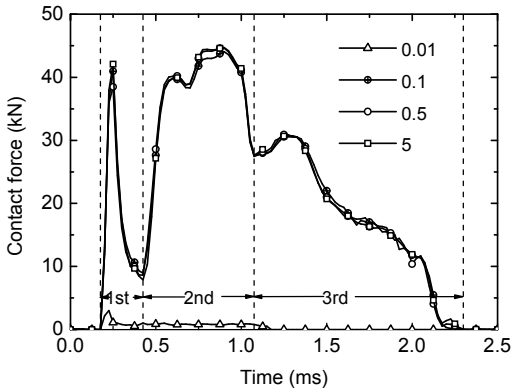

Fig. 19 Contact force for different contact penalty factor values

comparably stiff metal materials in this study, it is suggested that this value should be considered first to avoid false penetration or numerical instability in a metal blade/case containment simulation.

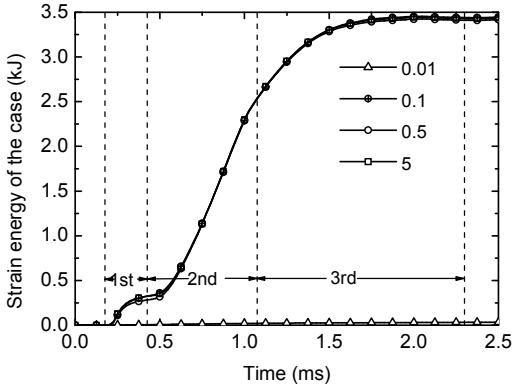

Fig. 20 Strain energy of the case for different contact penalty factor values

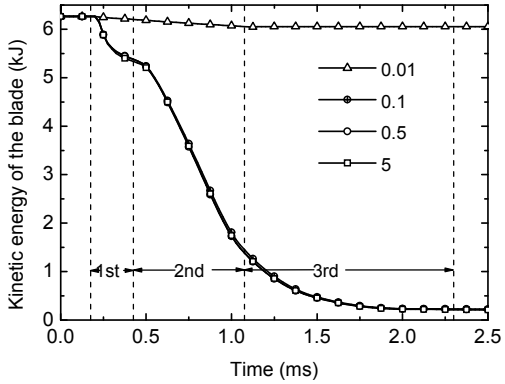

Fig. 21 Kinetic energy of the blade for different contact penalty factor values

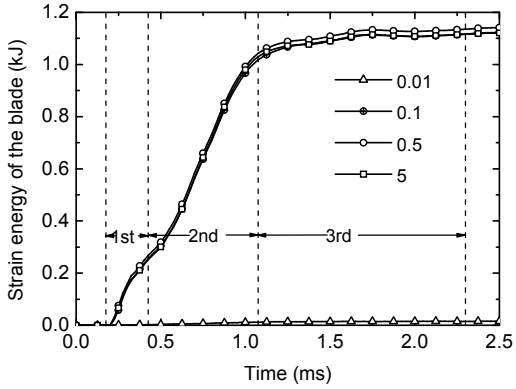

Fig. 22 Strain energy of the blade for different contact penalty factor values

3.6 Effect of friction coefficient

The friction coefficient, f, in the contact-impact algorithm of LS-DYNA is based on Coulomb formulation with an exponential interpolation function that can smooth the transition between the static,

f_s, and dynamic, f_d, coefficients of friction and can be expressed as

$$f = f_d + (f_s - f_d)e^{-c_d|v|}, \quad (6)$$

where v is the relative velocity and c_d is a decay constant. To simplify the friction coefficient expression, a constant friction coefficient was considered by setting f_s=f_d. According to the LS-DYNA Theory Manual, for mild steel on mild steel, the recommended friction coefficient was 0.57 (Hallquist, 2006). However, a value of 0.1 was proposed for metal working operations by Ravid and Bodner (1983). A very small value of 0.01 was suggested by Zukas (1990) for ballistic impacts involving metal-metal interfaces and a value of 0.05 was used for the lateral surfaces in ballistic impact situations (Borvik *et al.*, 2002). According to Goldsmith (1999), for non-ideal projectile impact on targets, a friction coefficient of 0.15 was introduced for thin steel plates, which is similar to the present work. In this section, the influences of friction coefficient were studied by setting different friction coefficient values for the same finite element model. The C3-3 model and the B2 model) were selected for the case and the blade, respectively. The value of the friction coefficient was set to 0, 0.05, 0.15 and 0.30 for the simulations, while the other parameters were kept the same as those in Section 3.3. Simulation results for different friction coefficient values are listed in Tables 11 and 12 and shown in Fig. 24.

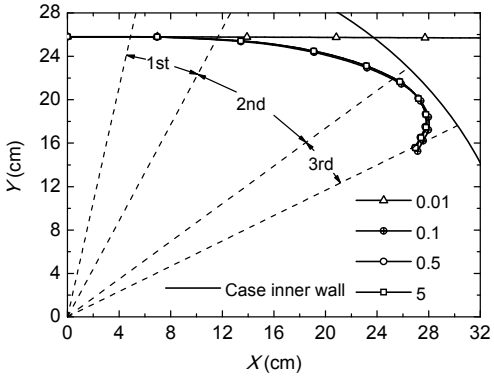

Fig. 23 Trajectories of the centroid of the blade in the *XY* plane for different contact penalty factor values

Variations of the selected parameters for different friction coefficient values are compared and given in Figs. 25–30. It is shown that simulation results are significantly affected by the friction

Table 11 Simulation results for different friction coefficient values

Value of friction coefficient	Kinetic energy (kJ)		Strain energy (kJ)		Perforation result of the case
	KE_{bi}	KE_{br}	IE_c	IE_b	
0	6.263	0.227	4.025	1.122	Circumferential tearing
0.05	6.263	0.104	3.856	1.106	Circumferential tearing
*0.15	6.263	0.224	3.447	1.123	Circumferential tearing
0.30	6.263	0.125	3.021	1.225	Circumferential tearing & tensile failure

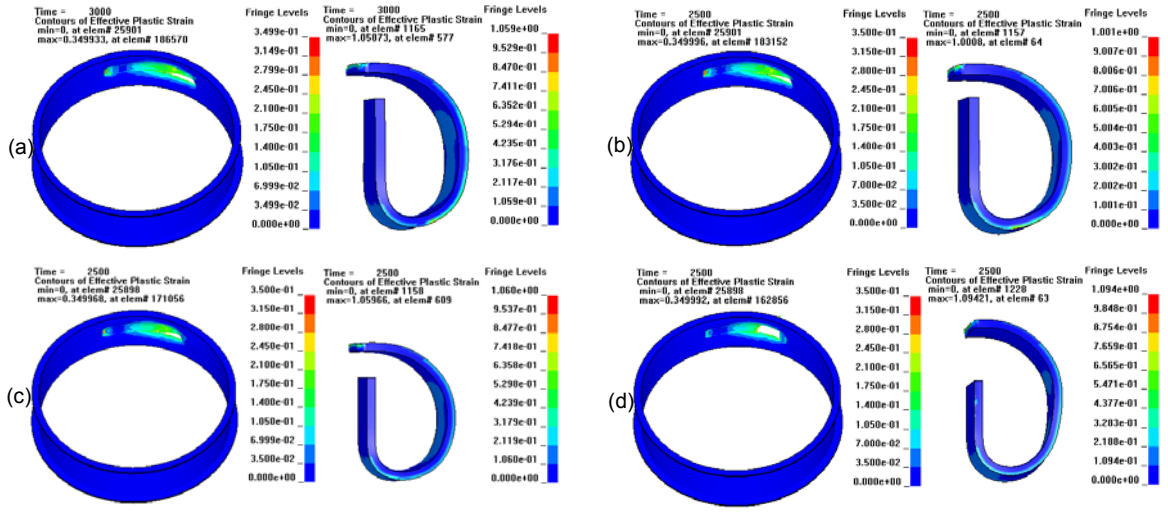

Fig. 24 Deformation and penetration results for different friction coefficient values of 0 (a), 0.05 (b), 0.15 (c) and 0.30 (d) (fringe level of plastic strain)

coefficient, especially larger than 0.15. For a larger friction coefficient value, the peak value of the contact force between the case and blade is smaller during the first stage and is larger during the second and third stages (Fig. 25). Lower kinetic energy level and shorter trajectory of the released blade, as shown in Fig. 27 and Fig. 29, are predicted due to higher level of the drag force exerted on the blade during the second stage. Moreover, the total strain energy absorbed by the case and the area of the impact zone with large plastic deformation decreases (Table 12), increasing the local density of the energy absorbed by the case and even causing tensile failure on the case for a value of 0.30 (Fig. 24). Not surprisingly, more sliding energy is dissipated between the contact surfaces and even reaches one fifth of the initial kinetic energy of the blade for a value of 0.30 (Fig. 30). For a value of 0.30, not only circumferential

Table 12 Comparison of the deformation and the failure on the case between the test and the numerical results

Test/Simulation	h_1 (mm)	h_2 (mm)	θ_p (°)	θ_{12} (°)	θ_t (°)
Test 1	7.0	25.0	56.4	40.5	16.3
0	8.6	25.3	63.1	44.3	21.8
0.05	7.7	24.7	59.7	44.6	20.7
*0.15	6.9	24.7	55.6	40.0	15.6
0.30	3.7	–	54.0	–	13.4

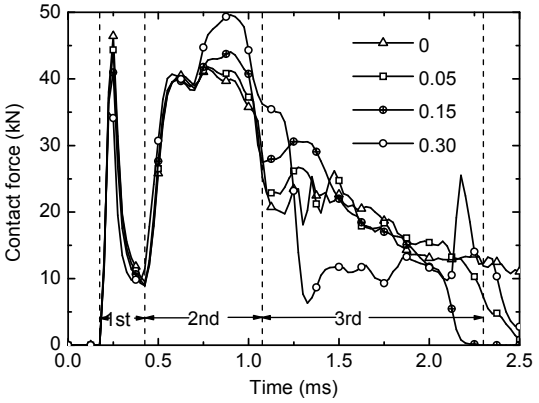

Fig. 25 Contact force between the case and the blade for different friction coefficient values

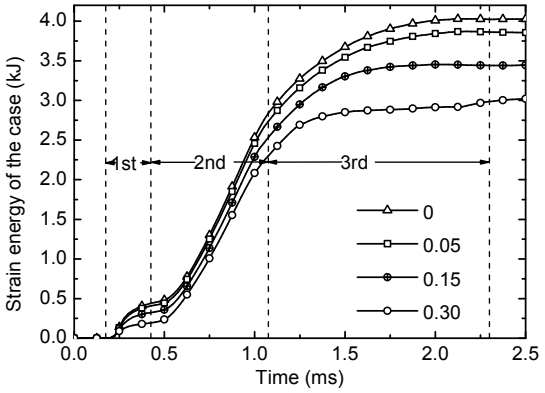

Fig. 26 Strain energy of the case for different friction coefficient values

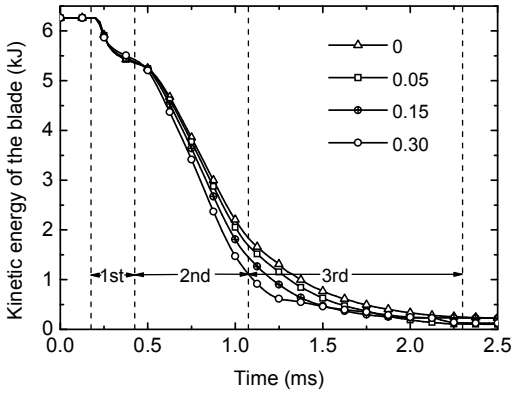

Fig. 27 Kinetic energy of the blade for different friction coefficient values

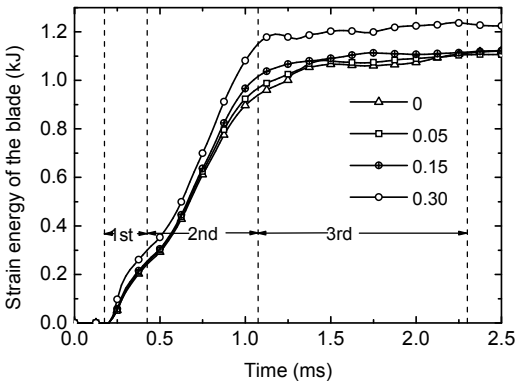

Fig. 28 Strain energy of the blade for different friction coefficient values

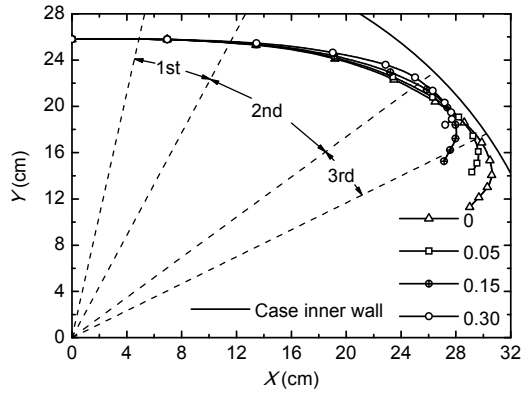

Fig. 29 Trajectories of the centroid of the blade in the *XY* plane for different friction coefficient values

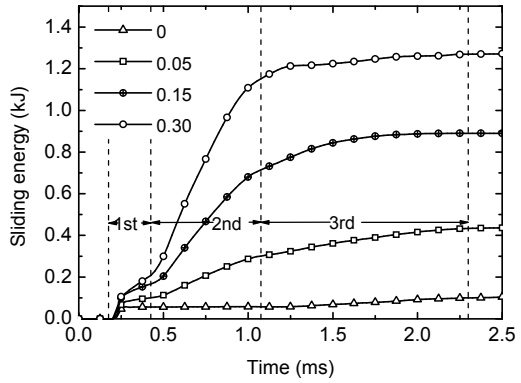

Fig. 30 Sliding energy for different friction coefficient values

tearing failure but also tensile failure of the separated band is predicted (Fig. 24).

In conclusion, the friction coefficient plays an important role in numerical simulation. It is suggested that the friction coefficient should be properly set according to actual conditions, such as the materials involved, and contact surface lubrications.

4 Applications of the simulation method

As mentioned in Section 2, there were a total of nine tests of single released blade impact on the cylindrical case. Based on the above discussions, the mesh pattern of the C3-3 model for the case and the mesh pattern of the B2 model for the released blade were used in the simulations for the other eight blade containment tests. To avoid false penetration, the contact penalty factor was set to 0.5. The friction coefficient was set to 0.15.

Final deformations and failures of the case and the released blade between the test and numerical results are compared in Fig. 31, where the numerical results are presented with fringe levels of plastic strain. Even though the physical mechanism governing the impact and plastic deformation process differ significantly between the tests, the plastic deformations of both the blade and the case are captured and described with good accuracy by the numerical simulations. Undoubtedly, there are still some small differences between the test and simulation results. However, it is well known that dynamic impact simulation not only depends on the finite element model and the contact-related parameters, but also strongly relies on the material relations that having proper constants which can describe the dynamic behavior of the material used in the tests. In addition, a number of incidental factors exist in the tests, which cannot be fully addressed in numerical simulations.

5 Conclusions

A numerical simulation method has been developed and validated to be used for steel blade/case impact and containment events such as an aeroengine fan or turbine blade released condition. The blade containment tests were carried out on a high-speed spin tester, and the simulations were implemented in LS-DYNA. One of the tests (Test 1) was used to evaluate the effects of the modeling-related factors, such as mesh density, contact penalty factor and friction coefficient, on the numerical results. It is found that the contact force, the energy translation and transformation, and the failure and deformation patterns predicted by the finite element models are strongly affected by these modeling-related factors. Based on the sensitivity study, a method general enough could be obtained for steel blade/case impact simulations. We can conclude that:

1. The more refined mesh for the impact zone of the case captures the localized elastoplastic deformation pattern of the case better. It predicts lower containment capacity of the case, less strain energy absorbed by the case, and smaller whole bending of the blade, which are closer to test results. At least three elements through the thickness of the case are needed to capture the detailed behaviors of the case.

2. The more refined mesh for the blade captures the localized bending deformation of the blade better. It predicts lower containment capacity of the case, more strain energy absorbed by the case, less strain energy absorbed by the blade and smaller whole bending of the blade. The element width size has a minimal influence on the simulation results due to the whole width of the blade contacting the case most of the time. The element size for the blade that equals to the element size in the impact zone of the case is refined enough because of the blade's higher material strength in this study. It is further suggested that a smaller element size should be used for a component with lower material strength.

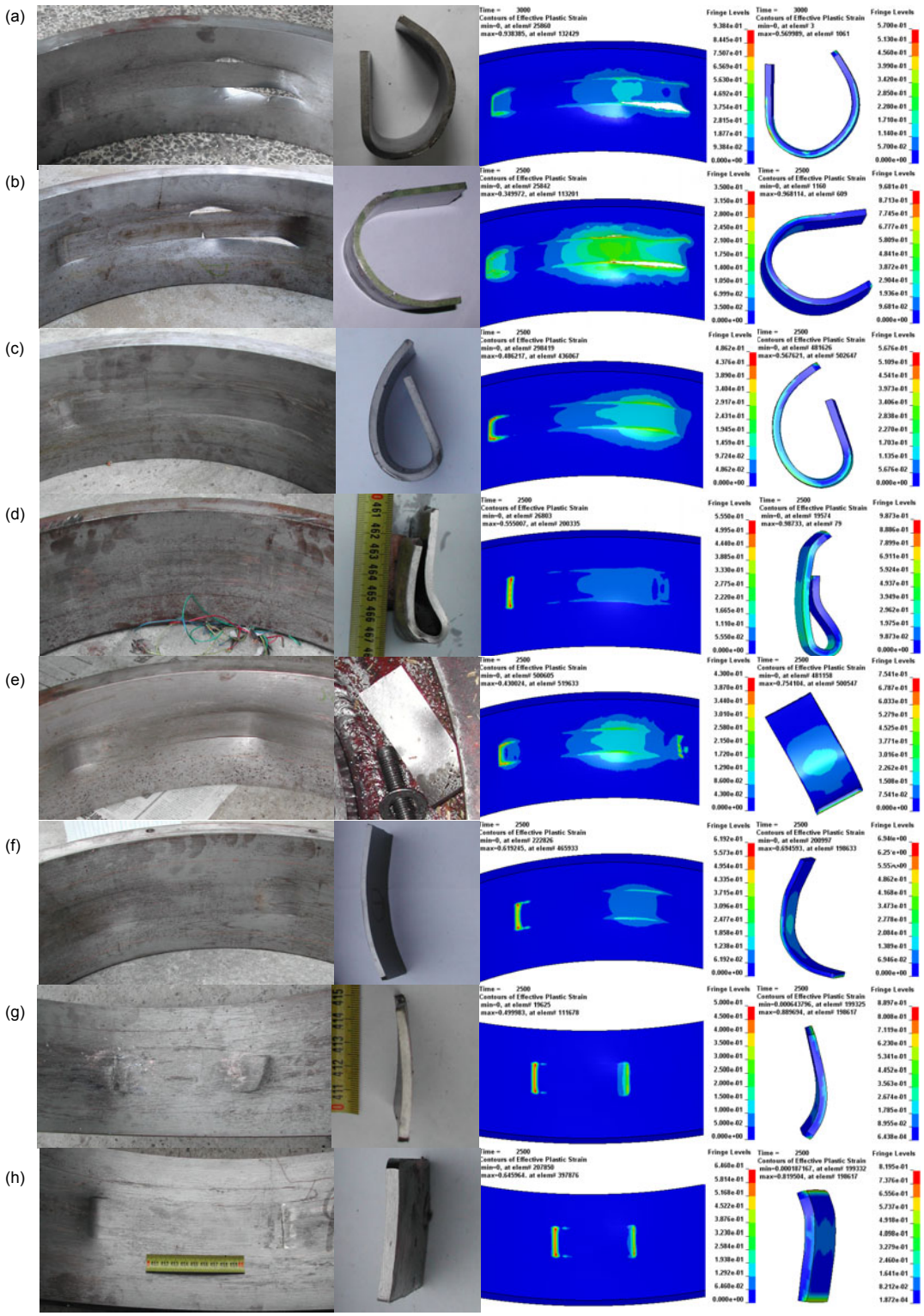

Fig. 31 Comparisons of the failure and deformation between the test and numerical results

(a) Test 2 (δ_c=2.1 mm, L=140 mm, b=40 mm, n_{off}=9416 r/min, E_k=5220 J); (b) Test 3 (δ_c=1.8 mm, L=140 mm, b=40 mm, n_{off}=8879 r/min, E_k=4644 J); (c) Test 4 (δ_c=3.0 mm, L=125 mm, b=40 mm, n_{off}=10585 r/min, E_k=6218 J); (d) Test 5 (δ_c=6.0 mm, L=115 mm, b=50 mm, n_{off}=13981 r/min, E_k=12871 J); (e) Test 6 (δ_c=2.7 mm, L=115 mm, b=40 mm, n_{off}=9473 r/min, E_k=4726 J); (f) Test 7 (δ_c=5.0 mm, L=105 mm, b=50 mm, n_{off}=11023 r/min, E_k=7499 J); (g) Test 8 (δ_c=5.0 mm, L=50 mm, b=50 mm, n_{off}=13389 r/min, E_k=6334 J); (h) Test 9 (δ_c=5.0 mm, L=40 mm, b=50 mm, n_{off}=13957 r/min, E_k=5686 J)

3. A smaller contact penalty factor might predict false penetration, and the numerical results predicted by larger ones will be almost the same. The default value of 0.1 always predicts reasonably good results.

4. The friction coefficient plays an important role in the simulation results. A larger value of the friction coefficient predicts smaller area with larger plastic deformation, less strain energy, and lower containment capacity of the case.

The numerical simulation method developed is verified by the experimental data and the numerical simulations for the other eight blade/case containment tests. Good agreements are obtained between the numerical and the experimental results. It seems that the numerical simulation approach developed in this study works well for steel blade/case containment analysis. However, further experimental work and simulation studies are needed to address some other influential factors, such as distortion geometry of a real fan or turbine blade, rotor whirling as a response of sudden unbalance, etc.

References

Ambur, D.R., Jaunky, N., Lawson, R.E., Knight, N.F.Jr, 2001. Numerical simulations for high-energy impact of thin plates. *International Journal of Impact Engineering*, **25**(7):683-702. [doi:10.1016/S0734-743X(00)00073-7]

Borvik, T., Hopperstad, O.S., Berstad, T., Langseth, M., 2002. Perforation of 12 mm thick steel plates by 20 mm diameter projectiles with flat, hemispherical and conical noses Part II: numerical simulations. *International Journal of Impact Engineering*, **27**(1):37-64. [doi:10.1016/S0734-743X(01)00035-5]

Carney, K.S., Lawrence, C., Carney, D.V., 2002. Aircraft Engine Blade-Out Dynamics. 7th International LS-DYNA Users Conference, Dearborn, USA. LSTC, California, USA, p.14-17.

Chen, G., Chen, Z.F., Tao, J.L., Niu, W., Zhang, Q.P., Huang, X.C., 2005. Investigation and validation on plastic constitutive parameters of 45 steel. *Explosion and Shock Waves*, **25**(5):451-456 (in Chinese).

Chen, G., Chen, Z.F., Xu, W.F., Chen, Y.M., Huang, X.C., 2007. Investigation on the J-C ductile fracture parameters of 45 steel. *Explosion and Shock Waves*, **27**(2):131-135 (in Chinese).

Cosme, N., Chevrolet, D., Bonini, J., Peseux, B., Cartraud, P., 2002. Prediction of Engine Loads and Damages Due to Fan Blade-Off Event. 43rd AIAA/ASME/ASCE/AHS/ASC Structures, Structural Dynamics, and Materials Conference, Denver, USA. AIAA, Virginia, USA, Report No. AIAA-2002-1666.

Dey, S., Borvik, T., Hopperstada, O.S., Langseth, M., 2007. On the influence of constitutive relation in projectile impact of steel plates. *International Journal of Impact Engineering*, **34**(3):464-486. [doi:10.1016/j.ijimpeng.2005.10.003]

Fan, Z.Q., Gao, D.P., Qin, Z.X., Jiang, T., 2006. Experimental study of 20# steel under tensile impact. *Gas Turbine Experiment and Research*, **19**(4):35-51 (in Chinese).

Goldsmith, W., 1999. Review: Non-ideal projectile impact on targets. *International Journal of Impact Engineering*, **22**(2-3):95-395. [doi:10.1016/S0734-743X(98)00031-1]

Hallquist, J.O., 2006. LS-DYNA Theoretical Manual. Livermore Software Technology Corporation, California, USA.

He, Q., Xuan, H.J., Liu, L.L., Hong, W.R., Wu, R.R., 2012. Perforation of aero-engine fan casing by a single rotating blade. *Aerospace Science and Technology*, in press. [doi:10.1016/j.ast.2012.01.010]

Heidari, M., Carlson, D.L., Sinha, S., Sadeghi, R., Heydari, C., Bayoumi, H., Son, J., 2008. An Efficient Multi-Disciplinary Simulation of Engine Fan-Blade out Event Using MD Nastran. 49th AIAA/ASME/ASCE/AHS/ASC Structures, Structural Dynamics, and Materials Conference, Schaumburg, USA. AIAA, Virginia, USA, Report No. AIAA-2008-2333.

Jain, R., 2010. Prediction of Transient Loads and Perforation of Engine Casing During Blade-Off Event of Fan Rotor Assembly. Proceedings of the IMPLAST Conference, Providence, USA.

Johnson, G.R., Cook, W.H., 1983. A Constitutive Model and Data for Metals Subjected to Large Strains, High Strain Rates and High Temperatures. Proceedings of the Seventh International Symposium on Ballistics, Hague, the Netherlands, p.541-547.

Johnson, G.R., Cook, W.H., 1985. Fracture characteristics of three metals subjected to various strains, strain rates, temperatures and pressures. *Engineering Fracture Mechanics*, **21**(1):31-48. [doi:10.1016/0013-7944(85)90052-9]

Knight, N.F.Jr, Jaunky, N., Lawson, R.E., Ambur, D.R., 2000. Penetration simulation for uncontained engine debris impact on fuselage-like panels using LS-DYNA. *Finite Elements in Analysis and Design*, **36**(2):99-133. [doi:10.1016/S0168-874X(00)00011-1]

Li, J.J., Xuan, H.J., Liao, L.F., Hong, W.R., Wu, R.R., 2009. Penetration of disk fragments following impact on thin plate. *Journal of Zhejiang University-SCIENCE A*, **10**(5):677-684. [doi:10.1631/jzus.A0820746]

Morris, A.J., Vignjevic, R., 1997. Consistent finite element structural analysis and error control. *Computer Methods in Applied Mechanics and Engineering*, **140**(1-2):87-108. [doi:10.1016/S0045-7825(96)01005-5]

Ravid, M., Bodner, S.R., 1983. Dynamic perforation of viscoplastic plates by rigid projectiles. *International Journal of Engineering Science*, **21**(6):577-591. [doi:10.1016/0020-7225(83)90105-2]

Sarkar, S., Atluri, S.N., 1996. Effects of multiple blade interaction on the containment of blade fragments during a rotor failure. *Finite Elements in Analysis and Design*,

23(2-4):211-223. [doi:10.1016/S0168-874X(96)80008-4]

Scheffler, D.R., Zukas, J.A., 2000. Practical aspects of numerical simulation of dynamic events: material interfaces. *International Journal of Impact Engineering*, **24**(8): 821-842. [doi:10.1016/S0734-743X(00)00003-8]

Shmotin, Y.N., Gabov, D.V., 2006. Numerical Analysis of Aircraft Engine Fan Blade-Out. 42nd AIAA/ASME/SAE/ASEE Joint Propulsion Conference & Exhibit, California, USA. AIAA, Virginia, USA, Report No. AIAA-2006-4620.

Sinha, S.K., Dorbala, S., 2009. Dynamic loads in the fan containment structure of a turbofan engine. *Journal of Aerospace Engineering*, **22**(3):260-269. [doi:10.1061/(ASCE)0893-1321(2009)22:3(260)]

Stallone, M.J., Gallardo, V., Storace, A.F., Bach, L.J., Black, G., Gaffney, E.F., 1983. Blade loss transient dynamic analysis of turbomachinery. *AIAA Journal*, **21**(8):1134-1138. [doi:10.2514/3.8216]

Teng, X., Wierzbicki, T., 2006. Evaluation of six fracture models in high velocity perforation. *Engineering Fracture Mechanics*, **73**(12):1653-1678. [doi:10.1016/j.engfracmech.2006.01.009]

Wierzbicki, T., Bao, Y., Lee, Y., Bai, Y., 2005. Calibration and evaluation of seven fracture models. *International Journal of Mechanical Sciences*, **47**(4-5):719-743. [doi:10.1016/j.ijmecsci.2005.03.003]

Xuan, H.J., Wu, R.R., 2006. Aeroengine turbine blade containment tests using high-speed rotor spin testing facility. *Aerospace Science and Technology*, **10**(6):501-508. [doi:10.1016/j.ast.2006.04.006]

Yu, C.L., Chen, Z.P., Wang, J., Yan, S.J, Yang, L.C., 2012. Effect of weld reinforcement on axial plastic buckling of welded steel cylindrical shells. *Journal of Zhejiang University-SCIENCE A (Applied Physics & Engineering)*, **13**(2):79-90. [doi:10.1631/jzus.A1100196]

Zukas, J.A., 1990. High Velocity Impact Dynamics. John Wiley & Sons, New York, USA.

Zukas, J.A., Scheffler, D.R., 2000. Practical aspects of numerical simulations of dynamic events: effects of meshing. *International Journal of Impact Engineering*, **24**(9): 925-945. [doi:10.1016/S0734-743X(00)00012-9]

Recommended reading

Li, Q., Liu, S.L., Zheng, S.Y., 2010. Rate-dependent constitutive model of poly(ethylene terephthalate) for dynamic analysis. *Journal of Zhejiang University-SCIENCE A (Applied Phsysics & Engineering)*, **11**(10): 811-816. [doi:10.1631/jzus.A1000182]

Xu, W.F., Huang, X.C., Hao, Z.M., Wang, Y., Xia, Y.M., 2010. Effect of the geometric shapes of specimens on impact tensile tests. *Journal of Zhejiang University-SCIENCE A (Applied Phsysics & Engineering)*, **11**(10):817-821. [doi:10.1631/jzus.A1000139]

Li, J.J., Xuan, H.J., Liao, L.F., Hong, W.R., Wu, R.R., 2009. Penetration of disk fragments following impact on thin plate. *Journal of Zhejiang University-SCIENCE A*, **10**(5): 677-684. [doi:10.1631/jzus.A0820746]

Zhang, T., Liu T.G., Zhao, Y., Luo, J.Z., 2004. Nonlinear dynamic buckling of stiffened plates under in-plane impact load. *Journal of Zhejiang University-SCIENCE*, **5**(5):609-617. [doi:10.1631/jzus.2004.0609]